1 **Title**

2 **Optogenetic relaxation of actomyosin contractility uncovers mechanistic roles of**

3 **cortical tension during cytokinesis.**

4

5 **Authors**

6 Kei Yamamoto[1,2,3], Haruko Miura[1,2], Motohiko Ishida[4,5], Satoshi Sawai[4,5], Yohei Kondo[1,2,3]*, and

7 Kazuhiro Aoki[1,2,3,6]*

8

9 **Affiliations**

10 [1]Division of Quantitative Biology, National Institute for Basic Biology, National Institutes of

11 Natural Sciences, 5-1 Higashiyama, Myodaiji-cho, Okazaki, Aichi 444-8787, Japan.

12 [2]Quantitative Biology Research Group, Exploratory Research Center on Life and Living Systems

13 (ExCELLS), National Institutes of Natural Sciences, 5-1 Higashiyama, Myodaiji-cho, Okazaki,

14 Aichi 444-8787, Japan.

15 [3]Department of Basic Biology, School of Life Science, SOKENDAI (The Graduate University for

16 Advanced Studies), 5-1 Higashiyama, Myodaiji-cho, Okazaki, Aichi 444-8787, Japan.

17 [4]Graduate School of Arts and Sciences, University of Tokyo, Komaba, 153-8902 Tokyo, Japan.

18 [5]Research Center for Complex Systems Biology, Universal Biology Institute, University of Tokyo,

19 Komaba, 153-8902 Tokyo, Japan.

20 [6]Lead Contact

21 *Co-corresponding authors

22 *Correspondence: y-kondo@nibb.ac.jp and k-aoki@nibb.ac.jp

23

24

27

Abstract

Actomyosin contractility generated cooperatively by nonmuscle myosin II and actin filaments plays essential roles in a wide range of biological processes, such as cell motility, cytokinesis, and tissue morphogenesis. However, it is still unknown how actomyosin contractility generates force and maintains cellular morphology. Here, we demonstrate an optogenetic method to induce relaxation of actomyosin contractility. The system, named OptoMYPT, combines a catalytic subunit of the type I phosphatase-binding domain of MYPT1 with an optogenetic dimerizer, so that it allows light-dependent recruitment of endogenous PP1c to the plasma membrane. Blue-light illumination was sufficient to induce dephosphorylation of myosin regulatory light chains and decrease in traction force at the subcellular level. The OptoMYPT system was further employed to understand the mechanics of actomyosin-based cortical tension and contractile ring tension during cytokinesis. We found that the relaxation of cortical tension at both poles by OptoMYPT accelerated the furrow ingression rate, revealing that the cortical tension substantially antagonizes constriction of the cleavage furrow. Based on these results, the OptoMYPT system will provide new opportunities to understand cellular and tissue mechanics.

INTRODUCTION

Actomyosin contractility underlies force generation in a wide range of cellular and tissue morphogenesis in animals. Prominent examples include the tail retraction of directionally migrating fibroblasts and the constriction of a contractile ring during cytokinesis (Green, Paluch, and Oegema 2012; Ridley et al. 2003). The actin-rich cell cortex, a thin network underneath the plasma membrane, is also relevant to the actomyosin contractility involved in maintaining cell morphology; namely, the actomyosin contractility at the cell cortex not only tunes mechanical rigidity, but also renders cells rapidly deformable as manifested in cell division and amoeboid migration (Kelkar, Bohec, and Charras 2020; Paluch, Aspalter, and Sixt 2016). Thus, it is of critical importance to disentangle the mode of action of actomyosin in order to understand how cells generate force and shape their morphology.

The actomyosin contractility in nonmuscle cells is mainly attributed to the force generated by nonmuscle myosin II (NMII) (Vicente-Manzanares et al. 2009). NMII contains two heavy chains, two essential light chains, and two regulatory light chains (Vicente-Manzanares et al. 2009; Heissler and Manstein 2013). The myosin regulatory light chains (MLCs) are phosphorylated by myosin light chain kinase (MLCK) and Rho-kinase (ROCK), thereby inducing conformational change in NMII and increasing its motor activity (Vicente-Manzanares et al. 2009). Small chemical

62   compounds have been widely used to perturb the actomyosin contractility, such as blebbistatin (an

63   inhibitor for NMII ATPase activity), Y-27632 (a ROCK inhibitor), and ML-7 (an MLCK inhibitor)

64   (Straight et al. 2003; Uehata et al. 1997; Saitoh et al. 1987). While these compounds have allowed

65   researchers to better understand the function of NMII, it is still technically challenging to control

66   their actions at the subcellular resolution because of their rapid diffusion.

67   　　　To overcome this limitation, recent efforts have been devoted to the development and

68   application of optogenetic tools to manipulate cell signaling related to actomyosin contractility

69   (Krueger et al. 2019). The most popular approach is to control the activity of RhoA, a member of

70   Rho family small GTPases. Light-induced recruitment of RhoGEF triggers RhoA activation, which

71   in turn activates ROCK and inactivates myosin light chain phosphatase (MLCP) (Wagner and

72   Glotzer 2016; Kimura et al. 1996; Valon et al. 2017) (Fig. 1a). These reactions eventually induce

73   myosin light chain phosphorylation, followed by an increase in the actomyosin contractility. It has

74   been reported that local accumulation of RhoGEF by light increases contractile force at the

75   subcellular scale (Wagner and Glotzer 2016; Oakes et al. 2017; Valon et al. 2017). These

76   technologies allow activation of NMII at the equator and the induction of partial constriction in

77   rounded cells in metaphase (Wagner and Glotzer 2016). Valon *et al.* further demonstrated that

78   trapping of overexpressed RhoGEF to the outer membrane of mitochondria resulted in a decrease in

79   actomyosin contractility (Valon et al. 2017). In addition, depletion of PI(4,5)P$_2$ at the plasma

80   membrane by optogenetic membrane translocation of 5-phosphatase OCRL has been shown to

81   modulate cell contractility and inhibit apical constriction during *Drosophila* embryogenesis

82   (Guglielmi et al. 2015). Although many of these tools enhance actomyosin contractility through

83   RhoA or phospholipids, tools that reduce actomyosin contractility below the basal level have not

84   yet been developed.

85   　　　Here, we report a new optogenetic tool to directly inactivate NMII; the system, called

86   OptoMYPT, is designed to recruit an endogenous catalytic subunit of type Ic phosphatase (PP1c) to

87   the plasma membrane with light, thereby dephosphorylating and inactivating NMII. We

88   demonstrate that MLCs are dephosphorylated and the traction force exerted by cells is reduced at

89   the local area where blue light was illuminated. Moreover, this system was applied to the mechanics

90   of cytokinesis to understand how and to what extent actomyosin-based cortical tension antagonizes

91   contractile ring tension and contributes to the cleavage furrow ingression rate.

92

93

94

95

3

96   **RESULTS**

97   **Design of an OptoMYPT system for reducing intracellular contractile force.**

98   To manipulate the intracellular contractile force, we focused on MLCP, which is composed of three

99   subunits, a catalytic subunit PP1c, a regulatory subunit (MYPT1), and a smaller subunit of 20-kDa

100   (M20) (Ito et al. 2004). MYPT1 contains a PP1c-binding domain (PP1BD) and myosin heavy chain

101   (MHC)-binding domain (Fig. 1b). MYPT1 holds PP1c through the PP1BD, and recruits it to NMII

102   to dephosphorylate MLC, leading to the inactivation of NMII. Phosphorylated MLC is mainly

103   localized near the plasma membrane such as at cortical actin and stress fibers, where the NMII

104   exerts mechanical force (Du and Frohman 2009).

105   Our strategy for the reduction of contractile force is based on inducing membrane

106   translocation of the PP1BD in MYPT1 with light, resulting in the co-recruitment of endogenous

107   PP1c at the plasma membrane and dephosphorylation of MLC. We refer to this system as the

108   OptoMYPT system. It has been reported that the 1 to 38 amino acids (a.a.) in the PP1BD are

109   particularly important for binding to PP1c, and that the 170 to 296 a.a. in the PP1BD serve as a

110   phosphorylated MLC-binding domain (Hirano, Phan, and Hartshorne 1997). As an optogenetic

111   switch in this study, we mainly employed the improved Light-Induced Dimer (iLID) system, which

112   binds to its binding partner, SspB, upon blue light illumination and dissociates from SspB under the

113   dark condition (Guntas et al. 2015). The iLID-based OptoMYPT system consists of a light-

114   switchable plasma membrane localizer, Stargazin-mEGFP-iLID, and an actuator, SspB-mScarlet-I-

115   PP1BD, which is translocated to the plasma membrane for the co-recruitment of the endogenous

116   PP1c with blue light (Fig. 1c). The Stargazin-mEGFP-iLID is suited for the subcellular protein

117   recruitment, because the large N-terminal transmembrane anchor limits the diffusion of SspB

118   proteins (Natwick and Collins 2021). Alternatively, we developed a cryptochrome 2 (CRY2)-based

119   OptoMYPT system, in which CRY2-mCherry-PP1BD was recruited to the plasma membrane with

120   blue light through binding to the plasma membrane localizer CIBN-EGFP-KRasCT (Kennedy et al.

121   2010).

122   We first compared the efficacy of light-induced membrane translocation between three

123   different lengths of PP1BDs: 1-38, 1-169, and 1-296 (hereafter referred to as MYPT38, MYPT169,

124   and MYPT296, respectively). In line with the previous study (Wu et al. 2005), SspB-mScarlet-I-

125   PP1BDs accumulated at the nucleus (Fig. S1a,b). To circumvent this problem, the nuclear export

126   signal (NES) was fused with the C terminus of the PP1BDs to export them to the cytoplasm (Fig.

127   S1a,b). As a control, we confirmed that Madin-Darby Canine Kidney (MDCK) cells exhibited the

128   translocation of SspB-mScarlet-I from the cytoplasm to the plasma membrane upon blue light

129   illumination (Fig. 1d,e). SspB-mScarlet-I-MYPT169 showed the best membrane translocation in

130   three differential lengths of PP1BDs (Fig. 1e; Movie S1). We recognized that a small fraction of

4

131   SspB-mScarlet-I-MYPT38 still resided in the nucleus (Fig. 1d, yellow arrowhead), and CRY2-

132   mCherry-MYPT38 formed aggregates and puncta in a blue light-dependent manner for an unknown

133   reason (Fig. S2). Next, we investigated whether PP1BDs of MYPT1 indeed bind to PP1c and

134   recruit it to the plasma membrane. In control cells, PP1c fused with miRFP703 (PP1c-miRFP703),

135   which was mainly localized at the nucleus, did not show any change in the subcellular localization

136   upon blue light illumination (Fig. 1d,f). As expected, SspB-mScarlet-I-MYPT38, -MYPT169, and -

137   MYPT296 demonstrated similar levels of translocation of PP1c-miRFP703 from the cytoplasm to

138   the plasma membrane upon blue light illumination (Fig. 1d,f; Movie S2). We further evaluated the

139   effect of overexpression of PP1BD on basal phosphorylation of MLC (ppMLC) by western blotting

140   analysis. Interestingly, MLCs were almost completely dephosphorylated in MYPT296-

141   overexpressing cells (Fig. S1c). Indeed, the cells expressing MYPT296 showed flattened

142   morphology with membrane protrusions similar to the morphology of cells treated with ROCK

143   inhibitor or myosin inhibitor (Worthylake and Burridge 2003; Totsukawa et al. 2004) (Fig. S1a).

144   This result is consistent with the previous report pointing out the existence of the ppMLC-binding

145   domain at the 170–296 a.a., which may facilitate recruitment of PP1BD to NMII and

146   dephosphorylation of MLC without any stimulation (Hirano, Phan, and Hartshorne 1997). Taken

147   together, these results led us to conclude that MYPT169 is well suited for the OptoMYPT system.

5
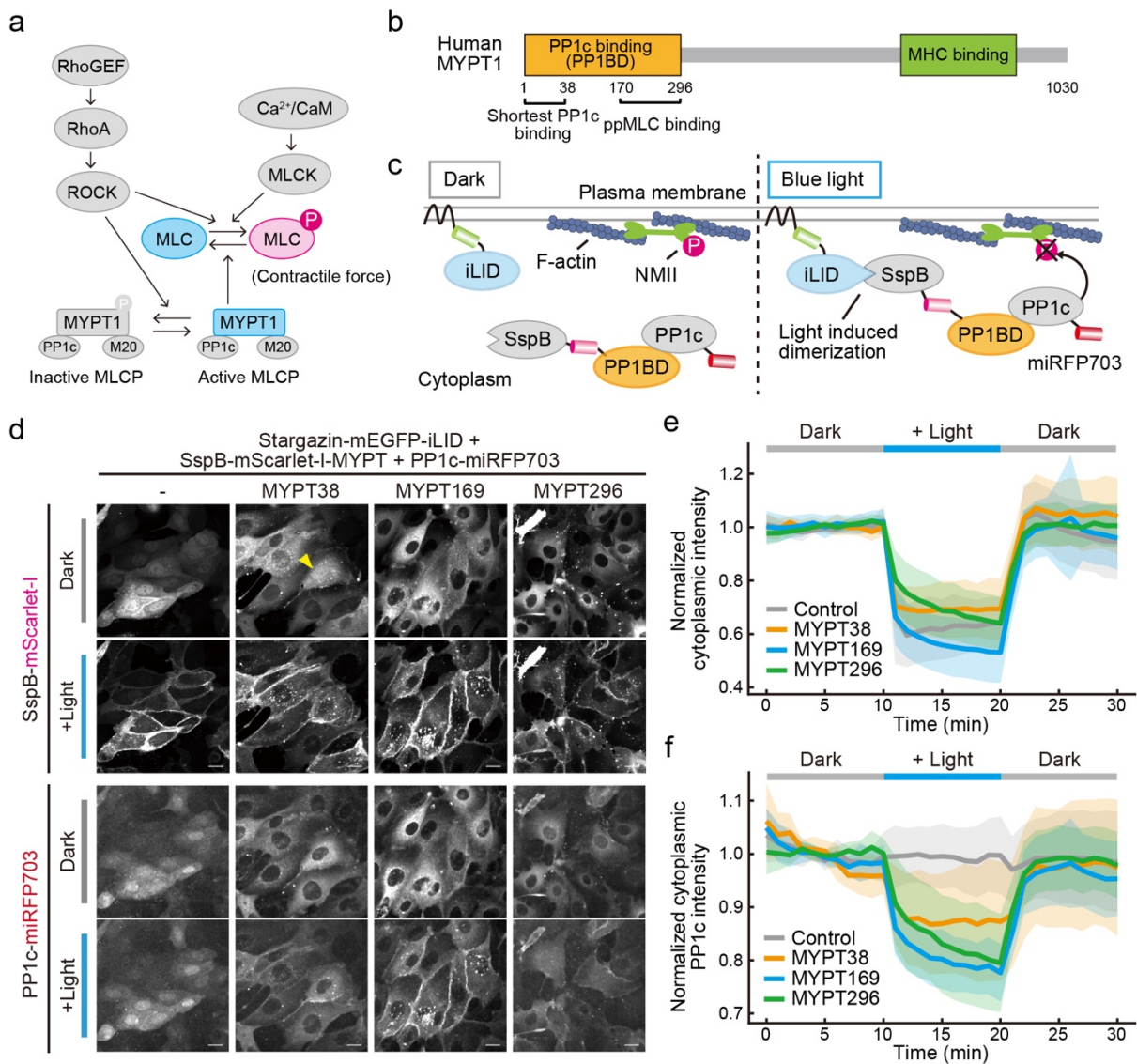
Figure 1. Development of the OptoMYPT system. (a) Schematic illustration of the signaling pathway for the regulation of MLC phosphorylation. (b) Domain structure of human MYPT1. (c) Schematic illustration of the OptoMYPT system. Stargazin-mEGFP-iLID is anchored to the plasma membrane. Upon blue light illumination, the SspB-mScarlet-I-fused PP1c-binding domain (PP1BD) of MYPT1 translocates to the plasma membrane along with endogenous PP1c, and inactivates NMII at the cell cortex. (d) Representative images of the SspB-mScarlet-I or the indicated SspB-mScarlet-I-PP1BDs of MYPT1 (upper two rows) and simultaneously expressing PP1c-miRFP703 (lower two rows) in MDCK cells under the dark condition (the first and third rows) and blue light condition (the second and fourth rows). Stargazin-mEGFP-iLID was also expressed as a localizer in all experiments. The yellow arrowhead indicates a cell showing nuclear accumulation of SspB-mScarlet-I-MYPT38. Scale bar, 20 μm. (e) Quantification of the cytoplasmic fluorescence change in mScarlet-I in panel d. The average values (bold lines) are plotted as a function of time with the SD. n = 15 cells. (f) Quantification of the cytoplasmic

162   fluorescence change in PP1c-miRFP703 in the indicated MDCK cells. The average values (bold

163   lines) are plotted as a function of time with the SD. n = 15 cells.

164

165

166   **Characterization of the OptoMYPT system.**

167   To evaluate whether the OptoMYPT dephosphorylates ppMLC in a blue light-dependent manner,

168   we directly stained ppMLC with immunofluorescence. The blue light was locally illuminated for 15

169   min, followed by fixation and immunofluorescence staining with the anti-ppMLC antibody (Fig.

170   2a). We herein adopted a CRY2-based OptoMYPT system (Kennedy et al. 2010), because the

171   slower dissociation kinetics of the CRY2-CIB system compared to that of the iLID-SspB system

172   was preferable for this experiment. Local illumination of blue light induced spatially restricted

173   recruitment of CRY2-mCherry and CRY2-mCherry-MYPT169 (Fig. 2b, right column). In addition,

174   the local recruitment of CRY2-mCherry-MYPT169, but not CRY2-mCherry, attenuated the

175   ppMLC signal (Fig. 2b, left column). The quantification of ppMLC fluorescence intensity in dark

176   and light illuminated areas (Fig. 2a) revealed a significant reduction in the ppMLC level (Fig. 2c).

177   The decrease in ppMLC by OptoMYPT prompted us to examine the effect on contractile

178   force by light. To do this, traction force microscopy was applied to randomly migrating MDCK

179   cells expressing the OptoMYPT system. The cells were seeded on polyacrylamide gel containing

180   infra-red fluorescence beads, so that we could infer the traction force by the displacement of

181   fluorescence beads and the mechanical properties of the polyacrylamide gel (Fig. 2d). The blue

182   light was locally focused on the lamellipodial region, where the cells were generating strong

183   traction force. SspB-mScarlet-I-MYPT169 was successfully recruited to the locally illuminated area

184   (Fig. 2e, upper). Under this condition, the traction force was reduced after blue light illumination

185   (Fig. 2e, lower; Fig. 2f, Movie S3). These results indicate that the OptoMYPT system can

186   dephosphorylate ppMLCs by local blue light illumination, leading to a reduction of traction force.

187

188
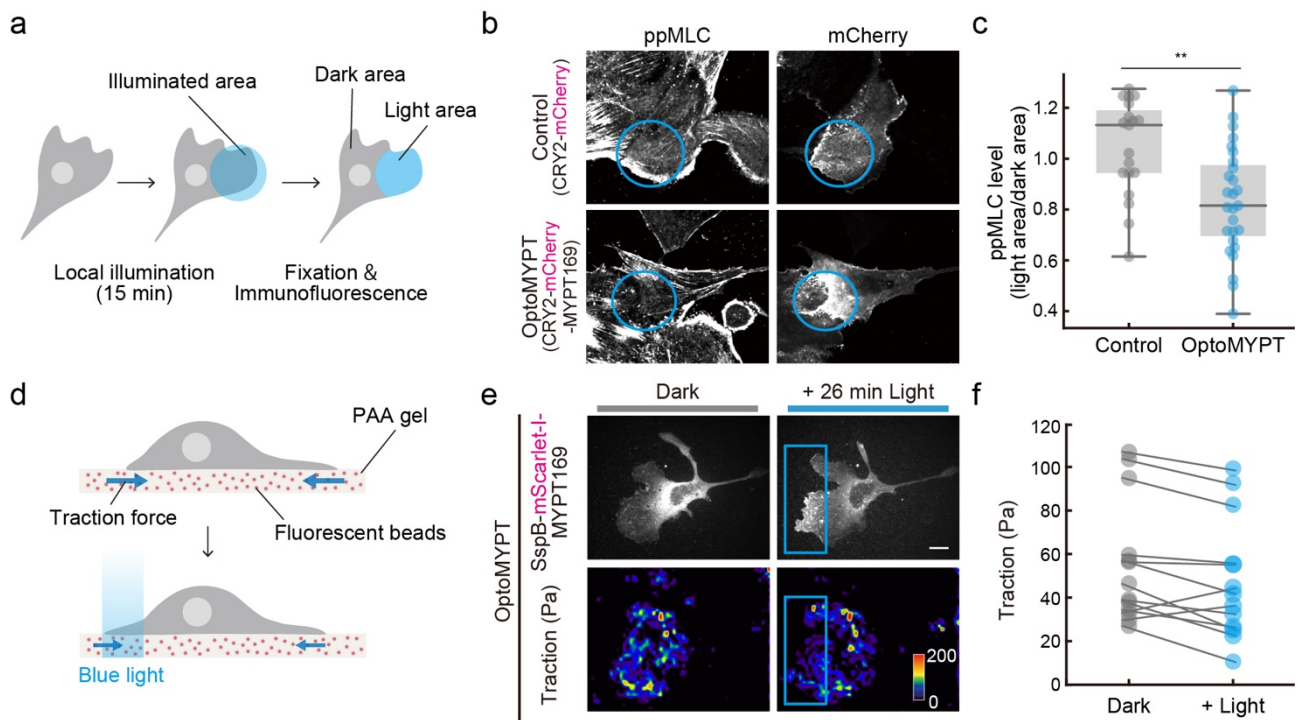
Figure 2. Characterization of the OptoMYPT system. (a) Schematic illustration of an experimental procedure to quantify ppMLC levels. The blue light was locally focused on the lamellipodial area in each cell, followed by fixation and immunostaining. (b) Immunofluorescence analysis of ppMLC after local blue-light illumination. The upper and lower images show MDCK cells expressing CRY2-mCherry and CRY2-mCherry-MYPT169, respectively. CIBN-EGFP-KRasCT was also expressed as a localizer in both experiments. Blue circles indicate the area illuminated with blue light. Scale bar, 10 μm. (c) The ppMLC level was quantified by dividing the mean fluorescence intensity of the light area by that of the dark area in panel a, and shown as a box plot, in which the box extends from the first to the third quartile with the whiskers denoting 1.5 times the interquartile range. n = 19 and 27 cells for the control and OptoMYPT, respectively. **p < 0.01 (student's t-test). (d) Schematic illustration of the traction force microscopy. (e) Traction force measurement in an MDCK cell expressing SspB-mScarlet-I-MYPT169 and Stargazin-mEGFP-iLID. Blue rectangles indicate blue-light illuminated areas. Traction force (Pa) is represented as a pseudo color. Scale bar, 20 μm. (f) Quantification of the traction force before and after blue-light illumination. n = 13 cells.

**Membrane protrusion induced by local dephosphorylation of ppMLC with OptoMYPT**

We next examined whether local dephosphorylation of ppMLC and reduction of contractile force have an impact on cell morphology by using OptoMYPT. The control MDCK cells that expressed SspB-mScarlet-I, Stargazin-mEGFP-iLID, and Lifeact-miRFP703 demonstrated local accumulation

8

211   of SspB-mScarlet-I by blue light illumination, but did not show morphological change (Fig. 3a). On

212   the other hand, the OptoMYPT-expressing MDCK cells reproducibly showed peripheral membrane

213   protrusions in the blue-light exposed area (Fig. 3b; Movie S4). We evaluated light-induced

214   membrane protrusion with a kymograph and time-course graph, which showed the movement of the

215   cell edge upon blue light illumination in OptoMYPT-expressing cells (Fig. 3c, d). The protruding

216   membrane was subsequently maintained under dark conditions. Interestingly, we often recognized

217   membrane retraction on the opposite side of the blue-light illumination area (Fig. 3e, arrowhead;

218   Movie S5). The OptoMYPT-induced membrane protrusion and retraction are consistent with the

219   previous reports showing Rac1 activation by inhibiting NMII or ROCK (Even-Ram et al. 2007;

220   Martin et al. 2016) and regulation of cell polarity by membrane tension (Houk et al. 2012).

221

222
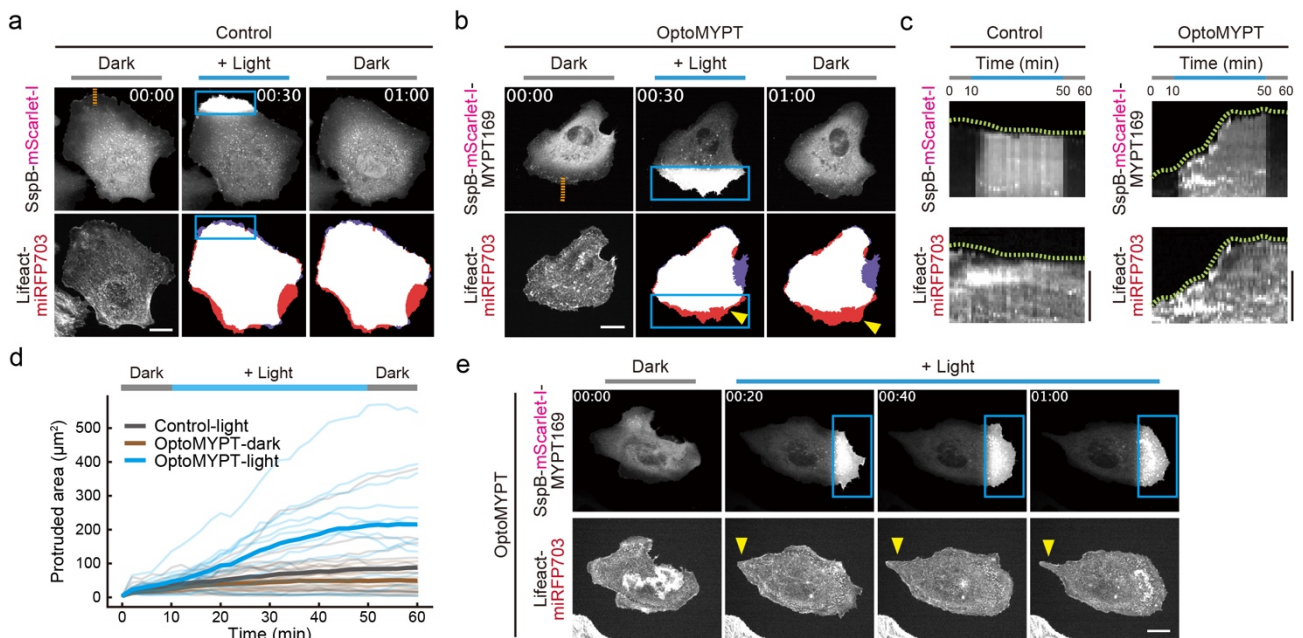
224   **Figure 3. Induction of membrane protrusion by the OptoMYPT system.** (a, b) Simultaneous

225   visualization of SspB-mScarlet-I (a) or SspB-mScarlet-I-MYPT169 (b) with F-actin (Lifeact-

226   miRFP703) in MDCK cells. Blue rectangles indicate blue-light illuminated areas. The middle and

227   right bottom images show binary images reconstructed from Lifeact-miRFP703 images; red and

228   purple areas represent protruding and retracting areas, respectively. The yellow arrowheads depict

229   membrane protrusion. Scale bar, 20 μm. (c) Kymographs were drawn along the orange dashed lines

230   in panels a and b. Green dashed lines show cell boundaries. Scale bar, 5 μm. (d) Quantification of

231   the local protruding areas under the indicated conditions. The total protruded area was calculated by

232   subtracting the cell area in the locally illuminated region at t = 0 from that at each time point. Local

233   blue light was illuminated from 10 to 50 min. The thin and bold lines indicate the individual and

234   averaged data, respectively. n = 15, 13, and 12 cells for Control-light (local blue light illumination),

9

235   OptoMYPT-dark (dark condition), OptoMYPT-light (local blue light illumination), respectively. (e)

236   Representative images of the induction of membrane retraction (yellow arrowhead) on the opposite

237   side of the blue-light illuminated area.

238

239

240   **Acceleration of the ingression rate of cleavage furrows during cytokinesis by the optical**

241   **relaxation of cortical tension.**

242   We next applied the OptoMYPT system to elucidate the mechanical regulation of the actin cortex

243   during cytokinesis. In this process, a contractile ring, which is mainly composed of F-actin and

244   NMII, transiently forms in the equatorial plane and generates tension to constrict the ring and divide

245   a cell into two daughter cells (Fig. 4a, solid arrows). The tension in the contractile ring is

246   counteracted by the tension generated by cortical actomyosin (Fig. 4a, dashed arrows). Recent

247   studies showed that genetic and pharmacological perturbations to the cortical actomyosin disrupted

248   proper cytokinesis (Taneja et al. 2020; Yamamoto et al. 2019; Sedzinski et al. 2011; O'Connell,

249   Warner, and Wang 2001), suggesting that the cortical tension plays a vital role. However, there is

250   still controversy in regard to the importance of cortical tension, because it is difficult to estimate the

251   strength of cortical tension relative to the contractile ring.

252   To address this issue, we perturbed the cortical tension by using the OptoMYPT system.

253   Blue light was locally and repeatedly illuminated at both poles from the onset of chromosome

254   segregation (Fig. 4a). SspB-mScarlet-I and SspB-mScarlet-I-MYPT169 were trapped in the polar

255   region (Control-pole and OptoMYPT-pole, respectively) (Fig. 4b; Movies S6, S7). Because the

256   overexpression of OptoMYPT might reduce basal actomyosin activity (Fig. S1c), cells expressing

257   SspB-mScarlet-I-MYPT169 under a dark condition throughout cytokinesis (OptoMYPT-dark) were

258   also used as a control (Fig. 4b; Movie S8).

259   To evaluate the reduction of cortical tension by local activation of the OptoMYPT, we

260   focused on the dynamics of membrane blebbing during cytokinesis (Fig. 4c). Because it has been

261   reported that high cortical tension causes membrane blebbing (Tinevez et al. 2009), we presumed

262   that the appearance of membrane blebbing and the number of blebs could be used as an indicator of

263   cortical tension. We counted the number of membrane blebs since the onset of cleavage furrow

264   ingression, and found a decrease in the number of blebs in OptoMYPT-pole cells as compared to

265   Control-pole and OptoMYPT-dark cells (Fig. 4c, d). This result is consistent with previous

266   observations, in which NMIIA-knockout or knockdown alleviated cortical tension during

267   cytokinesis (Yamamoto et al. 2019; Taneja et al. 2020). Furthermore, smaller membrane blebbing

268   emerged in Control-pole and OptoMYPT-dark cells from the early phase of cleavage furrow

269   ingression, and the number of blebs gradually increased as furrow ingressed, whereas OptoMYPT-

10

270   pole cells exhibited larger membrane blebbing from the late phase of cleavage furrow ingression

271   (Figs. 4e and S3). Based on these results, we concluded that the cortical tension in both poles

272   decreased through local application of the OptoMYPT system.

273   Finally, to estimate the strength of cortical tension relative to that of contractile ring tension,

274   we adapted a coarse-grained physical model describing the mechanics of cytokinesis (Sedzinski et

275   al. 2011; Yoneda and Dan 1972; Turlier et al. 2014). In this model, the furrow ingression rate (v) is

276   considered to be proportional to the difference between the contractile force of the ring (F_r) and the

277   resisting force exerted by the cortices (F_c), $v \propto F_r - F_c$ (see the Materials and Methods, Fig. S4, and

278   the Supplementary Discussion). Thus, we measured the furrow ingression rate under each

279   condition. The ingression rate of the cleavage furrow was significantly higher in OptoMYPT-pole

280   cells (2.26 ± 0.25 μm/min) than in Control-pole cells (1.55 ± 0.20 μm/min) and OptoMYPT-dark

281   cells (1.93 ± 0.33 μm/min) (Fig. 4f, g), indicating that the reduced cortical tension accelerates the

282   cleavage furrow ingression rate. These results highlight the negative contribution of the cortical

283   tension to the cleavage furrow ingression. Based on the coarse-grained physical model and

284   experimental data, we estimated that the cortical tension corresponds to at least 14.6% of the ring

285   tension during cytokinesis (see the Supplementary Discussion).

286

11
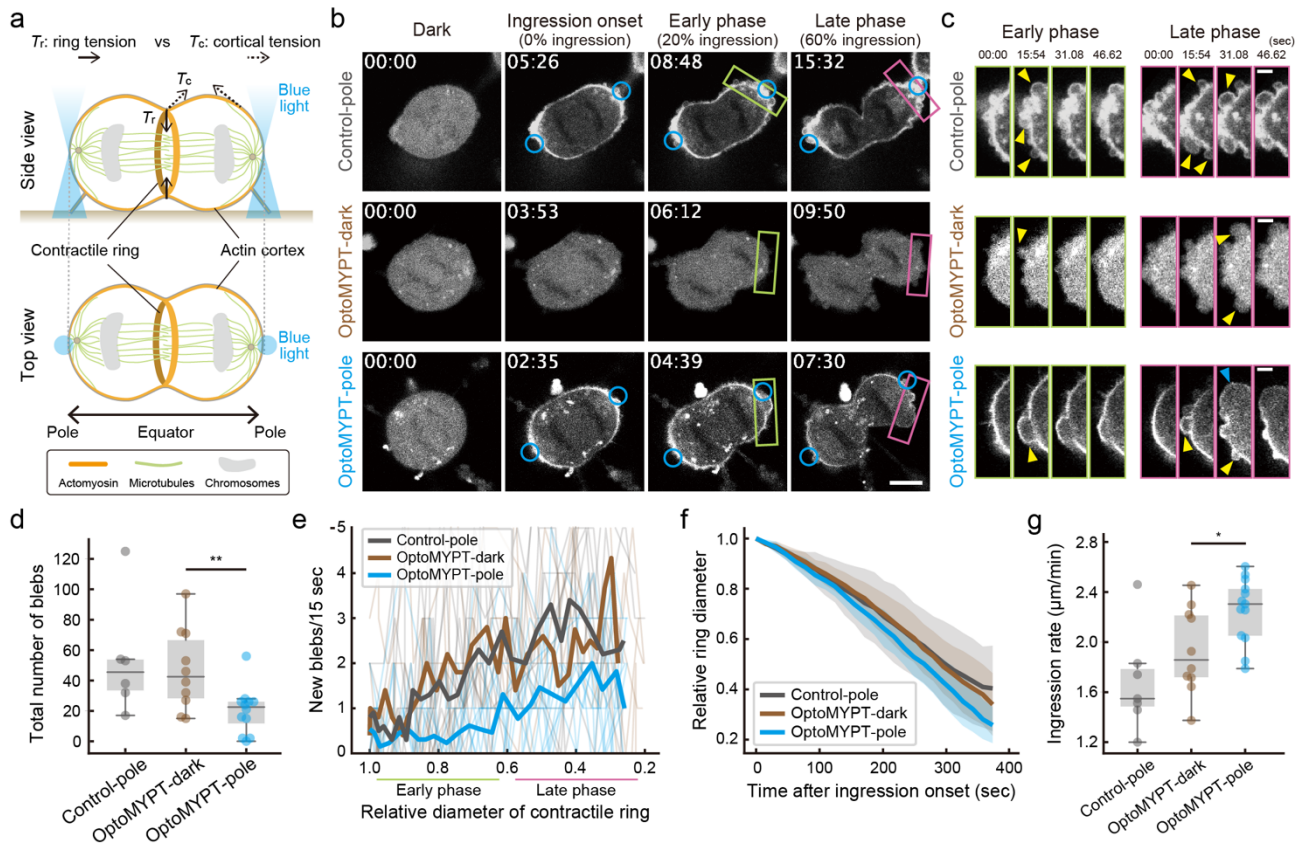
Figure 4. Examination of the actomyosin-based cortical tension during cytokinesis with OptoMYPT. (a) Schematic illustration of cytokinesis in animal cells. Solid and dashed arrows indicate ring tension and cortical tension, respectively. Orange, green, and gray objects indicate actomyosin, microtubules, and chromosomes, respectively. Blue light is focused on the poles on both sides. (b) Representative images of SspB-mScarlet-I (upper) or SspB-mScarlet-I-MYPT169 (middle and lower) in MDCK cells during cytokinesis. Blue circles in the upper and lower panels indicate blue-light illuminated areas. Middle panels represent cytokinesis of a cell under dark condition. Scale bar, 10 μm. (c) Inset images of polar blebbing (the green and magenta boxed regions in panel b, representing the early and late phases, respectively). Yellow and blue arrowheads indicate small and large new blebs per stack, respectively. Scale bar, 3 μm. (d, e) Quantification of the total number of blebs during cytokinesis, shown as a box plot (d), and of the number of new blebs emerged within 15.54 sec, shown as a line graph (e), in which thin and bold lines indicate individual and averaged data, respectively. n = 5, 10, and 13 cells for Control-pole, OptoMYPT-dark, and OptoMYPT-pole, respectively. **$p < 0.01$ (student's t-test). (f, g) Quantification of the furrow ingression rate after ingression onset. Averaged relative diameters are plotted as a function of time with the SD (f). The ingression rate was estimated by calculating the slope of the ingression rate from 1.0 to 0.6 in panel f, and shown as a box plot (g). n = 7, 10, and 13 cells for Control-pole, OptoMYPT-dark, and OptoMYPT-pole, respectively. *$p < 0.05$ (student's t-test).
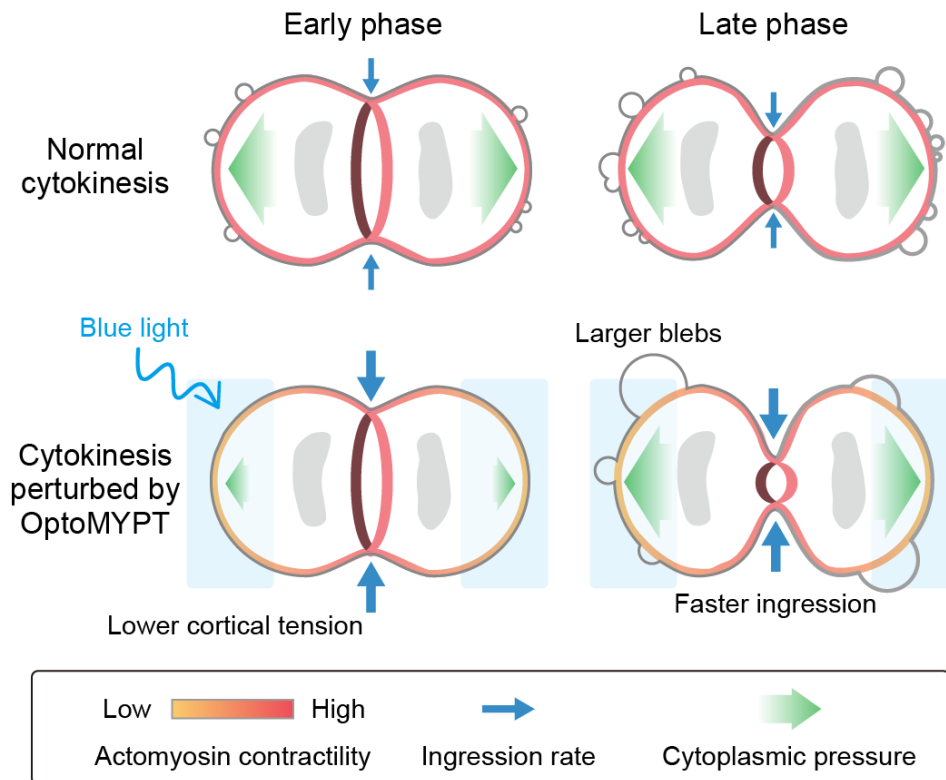
12

Figure 5. Schematic model of mechanical regulation of the contractile ring and the actin cortex during cytokinesis. In control cells, high cortical tension acts as a decelerator of the ring constriction. The high cortical tension and cytoplasmic pressure induce blebbing from the early phase of cytokinesis. The increased cytoplasmic pressure associated with ring constriction in the late phase is released by the increased number of blebs. In pole-illuminated OptoMYPT cells, the cleavage furrow ingression is accelerated due to the decrease in the cortical tension. As cleavage furrow ingression progresses, large blebs emerge due to the increased cytoplasmic pressure.

DISCUSSION

In this study, we developed a new optogenetic tool, OptoMYPT, and demonstrated light-dependent relaxation of cellular forces at the subcellular level. The OptoMYPT is substantially different from existing optogenetic tools related to the cell mechanics in two ways. First, the OptoMYPT reduces contractile forces below the basal level, and therefore provides additional flexibility for *in situ* control of actomyosin contractility and cellular morphology. Second, the OptoMYPT directly regulates NMII through MLC dephosphorylation, whereas optogenetic modulation of RhoA activity or PI(4,5)P$_2$ may affect pathways other than NMII, since RhoA and PI(4,5)P$_2$ are known to control various downstream effectors such as ROCK, mDia, and the ezrin-radixin-moesin (ERM) proteins (Oshiro, Fukata, and Kaibuchi 1998; Yonemura et al. 2002; Narumiya, Tanji, and Ishizaki 2009).

13

328   Using the OptoMYPT system, we experimentally revealed the negative contribution of the

329   cortical tension to the cleavage furrow ingression rate during cytokinesis; *i.e.*, the decrease in

330   cortical tension at both poles by OptoMYPT accelerates furrow ingression (Figs. 4 and 5). It has

331   been reported that the reduction of cortical tension by laser ablation in the polar region decelerates

332   cleavage furrow ingression in cytokinesis of *C. elegans* embryos (Khaliullin et al. 2018). This

333   discrepancy could be due to the difference in the force balance between the pole and equator; in *C.*

334   *elegans* embryos, NMII is actively removed from the polar region and accumulates at the equator

335   due to the cortical flow, and thus cortical tension is much weaker than ring tension (Chapa-Y-Lazo

336   et al. 2020; Reymann et al. 2016). Meanwhile, our results indicate that cortical tension in cultured

337   mammalian cells is comparable to contractile ring tension (Fig. 4), which is in good agreement with

338   the previous work (Sedzinski et al. 2011). Such a high cortical tension is advantageous because it

339   confers shape stability to mitotic cells (Sedzinski et al. 2011). This has been corroborated in a

340   recent paper demonstrating that high cortical stiffness in cancer cells allows them to divide in a

341   confined environment (Matthews et al. 2020). The benefit of cortical tension is not required in *C.*

342   *elegans* embryos, because they are covered and protected by a rigid eggshell. However, high

343   cortical tension is a double-edged sword, because excessive cortical tension induces cytokinetic

344   shape oscillation and abscission failure (Mukhina, Wang, and Murata-Hori 2007; Taneja et al.

345   2020; Girard et al. 2004). The estimated cortical tension relative to ring tension (F_c/F_r), ~14.6%,

346   may achieve a balance between morphological maintenance and timely cytokinesis.

347   We also focused on the dynamics of membrane blebbing during cytokinesis (Fig. 4).

348   Although the functional significance of blebbing is poorly understood, except in relation to cell

349   migration, the mechanisms underlying membrane blebbing have been increasingly reported.

350   Membrane blebbing is initiated by local rupture of the actin cortex and/or detachment of the actin

351   cortex from the plasma membrane (Charras and Paluch 2008). The growth of membrane blebs

352   requires a condition under which hydraulic pressure caused by actomyosin-based cortical tension

353   overcomes plasma membrane tension (Tinevez et al. 2009). We showed that numerous small blebs

354   emerged in the "early phase" of furrow ingression in control MDCK cells, and these were

355   suppressed by relaxation of cortical tension with OptoMYPT (Figs. 4e, 5, and S3). This

356   phenomenon is clearly consistent with the aforementioned mechanisms. Meanwhile, MDCK cells

357   expressing OptoMYPT exhibited large blebs in the "late phase" of cleavage furrow ingression when

358   both poles were illuminated with blue light (Figs. 4 and 5). The late onset of blebbing in the pole-

359   illuminated cells probably occurs because the progression of cleavage furrow ingression raises

360   hydraulic pressure, and thereby induces detachment of the actin cortex from the plasma membrane,

361   leading to the pressure release through bleb formation. To the best of our knowledge, the mechanics

362   of bleb formation in the "late phase" of the furrow ingression are a hitherto unrecognized process.

363   There still remain some issues to be addressed with respect to the OptoMYPT. First is the

364   issue of substrate specificity in OptoMYPT. We could not exclude the possibility that the

365   OptoMYPT dephosphorylates additional substrates other than MLC. However, based on the fact

366   that the OptoMYPT activation at both poles during cytokinesis did not induce bleb formation, it is

367   unlikely that OptoMYPT dephosphorylates and inactivates the ERM proteins cross-linking the

368   plasma membrane and actin cortex to prevent membrane bleb formation (Rodrigues et al. 2015).

369   The next issue is the localizer of optogenetic switches. In the current OptoMYPT system,

370   dephosphorylation of MLC was induced by recruiting MYPT169 to the plasma membrane upon

371   illumination with blue light. However, it is plausible that the OptoMYPT dephosphorylates and

372   inactivates only the NMII existing in the vicinity of the plasma membrane, and not the NMII in the

373   other subcellular locations. The use of a localizer that is closer to endogenous active NMII or a

374   specific localization such as the apical membrane of epithelial cells could result in an OptoMYPT

375   system with better specificity and spatial resolution than the current version.

376   The OptoMYPT system will provide opportunities not only to understand the mechanics of

377   morphogenesis, but also to shape the morphology of cells and tissues with precision and flexibility

378   as desired. Recent papers have applied optogenetic systems *in vivo*, and succeeded in inducing

379   arbitrary forms of the apical constriction (Izquierdo, Quinkler, and De Renzis 2018). By combining

380   red light-responsive optogenetic tools such as PhyB-PIF with blue light-responsive tools (Levskaya

381   et al. 2009; Uda et al. 2017), it will be possible to create more sophisticated morphology with an

382   increase or decrease in contractile force in the same cells and tissues.

383

384

Materials and Methods

Plasmids

387   The cDNAs of human MYPT1 and PP1c were derived from HeLa cells (Human Science Research

388   Resources Bank). SspB-mScarlet-I-PP1BDs were obtained by Gibson assembly cloning, combining

389   the SspB obtained from pPBbsr tgRFPt-SspB and cDNAs of PP1BDs. Stargazin-mEGFP-iLID was

390   obtained by Gibson assembly cloning, combining the Stargazin derived from Stargazin-GFP-

391   LOVpep (plasmid #80406: Addgene) and pPBbsr Venus-iLID-CAAX. CRY2 and CIBN-EGFP-

392   KRasCT were obtained from pCX4puro-CRY2-CRaf and pCX4neo-CIBN-EGFP-KRasCT (Aoki et

393   al. 2013) and inserted into the pCAGGS vector (Niwa, Yamamura, and Miyazaki 1991). The

394   cDNAs of Lifeact and NES were obtained by oligo DNA annealing and ligation, and inserted into

395   each vector. The cDNA of hyPBase, an improved PiggyBac transposase (Yusa et al. 2011), was

396   synthesized (FASMAC), and inserted into the pCAGGS vector. The nucleotide sequences of newly

397   generated constructs are provided in Table S1.

398

Cell culture

400 MDCK cells (no. RCB0995: RIKEN Bioresource Center) were maintained in minimal essential

401 medium (MEM; 10370-021: ThermoFisher Scientific) supplemented with 10% fetal bovine serum

402 (FBS; 172012-500ML: Sigma), 1x Glutamax (35050-061: ThermoFisher), and 1 mM sodium

403 pyruvate (11360070: ThermoFisher) in a 5% CO_2 humidified incubator at 37°C. The cells were

404 split as previously reported (Aoki et al. 2017).

405

Transfection

407 Because PP1BDs of MYPT1 fused with fluorescent proteins tend to aggregate for long-term

408 expression, most experiments were performed by transient expression. The MDCK cells were

409 electroporated by using Nucleofector IIb (Lonza) according to the manufacturers' instructions (T-

410 023 program) with a house-made DNA- and cell-suspension solution (4 mM KCl, 10 mM $MgCl_2$,

411 107 mM Na_2HPO_4, 13 mM NaH_2PO_4, 11 mM HEPES pH. 7.75). After electroporation, the cells

412 were plated on collagen-coated 35-mm glass-base dishes.

413

Establishment of stable cell lines

415 For transposon-mediated gene transfer, MDCK cells were transfected with PiggyBac donor vectors

416 and PiggyBac transposase-expressing vectors at a ratio of 3:1. One day after transfections, cells

417 were treated with 10 μg/mL blasticidin S (InvivoGen, San Diego, CA) or 1.0 μg/mL puromycin

418 (InvivoGen) for selection. The bright bulk cell population was collected using a cell sorter (MA900;

419 SONY).

420

Live-cell fluorescence imaging

422 Cells were imaged with an IX83 inverted microscope (Olympus, Tokyo) equipped with an sCMOS

423 camera (Prime: Photometrics, Tucson, AZ; or ORCA-Fusion BT: Hamamatsu Photonics,

424 Hamamatsu, Japan), a spinning disk confocal unit (CSU-W1; Yokogawa Electric Corporation,

425 Tokyo), and diode lasers at wavelengths of 488 nm, 561 nm, and 640 nm. An oil immersion

426 objective lens (UPLXAPO60XO, N.A. 1.42; Olympus) or an air/dry objective lens

427 (UPLXAPO40X, N.A. 0.95; Olympus) was used. The excitation laser and fluorescence filter

428 settings were as follows: Excitation laser, 488 nm (mEGFP), 561 nm (mScarlet-I), and 640 nm

429 (miRFP703); dichroic mirror, DM 405/488/561 dichroic mirror (mEGFP, mScarlet-I, and

430 miRFP703); emission filters, 500–550 nm (mEGFP), 580–654 nm (mScarlet-I), and 665–705 nm

431 (miRFP703). During observation, cells were incubated with a stage incubator set to 37 °C and

432 containing 5% CO_2 (STXG-IX3WX; Tokai Hit).

16

433   For global illumination of the blue light, blue LEDs (450 nm) were manually illuminated

434   from the top of the stage or pulsed blue light (488 nm) was illuminated through the objective lens.

435   For local light illumination in the interphase cells, a digital micromirror device (Polygon 400;

436   Mightex) mounted on the IX83 microscopic system, and pT-100 (CoolLED) were used. For local

437   light illumination during cytokinesis, an SP8 FALCON inverted confocal laser scanning

438   microscope (Leica) equipped with a water immersion objective lens (HC PL APO 63x/1.20 W

439   motCORR; Leica) was used. Local light illumination was started using the FRAP function just after

440   chromosome segregation onset. We illuminated every 3.11 sec, and acquired images every 15.54

441   sec. The positions of regions of interest (ROIs) were manually corrected every 2 min in all samples.

442   For all time-lapse imaging, MDCK cells were plated on 35 mm glass-base dishes (IWAKI).

443   Before time-lapse imaging, the medium was replaced with FluoroBrite (Invitrogen) supplemented

444   with 10% FBS, 1x Glutamax.

445

446   **Immunofluorescence**

447   Cells were fixed with 3.7% formaldehyde in PBS for 20 min, followed by permeabilization by 5

448   min incubation in 0.05% Triton X-100-containing PBS. Samples were soaked for 30 min in Can

449   Get Signal immunostain (solution A) (Toyobo, Japan), and then incubated with ppMLC antibody

450   (1:50 dilution; Cell Signaling Technology #3674) in Can Get Signal immunostain (solution A) for 1

451   h at room temperature. Next, the cells were washed 3 times with PBS, and then incubated for 1 h at

452   room temperature with Alexa 555-conjugated anti-rabbit IgG (1:100 dilution; ThermoFisher) in Can

453   Get Signal immunostain (solution A). Finally, the cells were washed 3 times with PBS and

454   subjected to fluorescence imaging.

455

456   **Traction force microscopy**

457   Polyacrylamide gel substrates were prepared in accordance with previously published protocols

458   (Tambe et al., 2011; Trepat et al., 2009). In brief, the gel solution was prepared with 4%

459   acrylamide, 0.1% bisacrylamide, 0.8% ammonium persulfate, 0.08% TEMED (Nacalai Tesque),

460   and 5% deep red fluorescent carboxylate-modified beads (0.2 μm diameter; F8810; Thermo Fisher

461   Scientific). 13 μL of the mixture was added to a 35 mm glass-base dish (IWAKI) and then covered

462   with a glass coverslip of 15 mm diameter (Matsunami). After gel polymerization at room

463   temperature, the surface was coated with 0.3 mg/mL type I collagen (Nitta Gelatin, Osaka, Japan)

464   using 4 mM sulphosuccinimidyl-6-(4-azido-2-nitrophenylamino) hexanoate (Sulfo-SANPAH;

465   Pierce). Cells were seeded on the gel, and imaged with a spinning disk confocal microscope. To

466   quantify the traction force, two Fiji plugins, *i.e.*, the iterative PIV and FTTC plugins, were used.

17

467 Note that Young's modulus of the gel was estimated as ~2 kPa according to a previous report (Tse

468 and Engler 2010). The traction force in locally illuminated areas was used for the quantification.

469

470 **Immunoblotting**

471 Cells were lysed in 1x SDS sample buffer. After sonication, the samples were separated by 5–20%

472 gradient SDS-polyacrylamide gel electrophoresis (Nagaiki precast gels; Oriental Instruments, Ltd.)

473 and transferred to polyvinylidene difluoride membranes (Millipore). After blocking with Odyssey

474 Blocking Buffer-TBS (LICOR Biosciences) for 1 h, the membranes were incubated with primary

475 antibodies overnight at 4°C, followed by the secondary antibodies for 1 h at room temperature. For

476 primary antibodies, ppMLC antibody (1:500 dilution; Cell Signaling Technology #3674), phospho-

477 Ezrin/Radixin/Moesin antibody (1:500 dilution, Cell Signaling Technology #3276), and α-Tubulin

478 antibody (DM1A) (1:5000 dilution; sc-32293: Santa Cruz Biotechnology) were diluted in Odyssey

479 Blocking Buffer-TBS. For secondary antibodies, IRDye680LT-conjugated goat polyclonal anti-

480 rabbit IgG (H + L) (1:5000 dilution; LI-COR Bioscience) and IRDye800CW-conjugated donkey

481 polyclonal anti-mouse IgG (H + L) (1:5000 dilution; LI-COR Bioscience) were diluted in Odyssey

482 Blocking Buffer-TBS. Proteins were detected with an Odyssey infrared scanner (LI-COR

483 Bioscience).

484

485 **Imaging analysis**

486 All fluorescence imaging data were analyzed and quantified by Fiji (Image J). For all images, the

487 background was subtracted and images were registered by StackReg, a Fiji plugin to correct

488 misregistration, if needed. To quantify the cytoplasmic fluorescence intensity changes in Figure 1,

489 the ROI was selected in each image and normalized by the mean fluorescence intensity of the first

490 10 images under the dark condition. To quantify the area of membrane protrusion in Figure 3, the

491 ROI was chosen so as to coincide with the local light-irradiated area. In OptoMYPT-dark cells, the

492 ROI was a region of lamellipodia similar to that of light-illuminated cells. Fluorescence images of

493 Lifeact-miRFP703 were binarized and the difference between the area at each time point and at t =

494 0 was calculated.

495

496 **Physical modeling**

497 According to previous modeling efforts on the force balance in a dividing cell (Sedzinski et al.

498 2011; Yoneda and Dan 1972), the temporal change in radius of the contractile ring, R_r, is described

499 as

500 $$\alpha \frac{dR_r}{dt} = -(T_r - 2R_r T_c \cos\theta) \qquad - (1),$$

18

501   where α is ring viscosity, T_r is the tension of the contractile ring, T_c is the tension in the actomyosin

502   cortex, and θ is the angle between the equatorial plane and polar surface at the furrow (see Fig. S4

503   for the details). Note that our model was simplified from Eq. S1 in the report of (Sedzinski et al.

504   2011), since we consider symmetric pole shapes. For brevity, let F_r and F_c denote T_r (ring tension)

505   and $2R_r T_c \cos\theta$ (cortical tension), respectively (Fig. S4). Then, the furrow ingression rate, v, can be

506   expressed as

507
$$v \propto F_r - F_c. \qquad \text{- (2)}$$

508

509

Acknowledgments

518

519

Author contributions

521   K.Y. and K.A. designed the research. K.Y., H.M., M.I. and S.S. performed experiments. K.Y. and

522   H.M. analyzed data. K.Y., Y.K., and K.A. wrote the manuscript.

523

524

Declaration of Interests

526   The authors declare no competing interests.

References

Aoki, Kazuhiro, Yohei Kondo, Honda Naoki, Toru Hiratsuka, Reina E. Itoh, and Michiyuki Matsuda. 2017. "Propagating Wave of ERK Activation Orients Collective Cell Migration." *Developmental Cell* 43 (3): 305–17.e5.

Aoki, Kazuhiro, Yuka Kumagai, Atsuro Sakurai, Naoki Komatsu, Yoshihisa Fujita, Clara Shionyu, and Michiyuki Matsuda. 2013. "Stochastic ERK Activation Induced by Noise and Cell-to-Cell Propagation Regulates Cell Density-Dependent Proliferation." *Molecular Cell* 52 (4): 529–40.

Chapa-Y-Lazo, Bernardo, Motonari Hamanaka, Alexander Wray, Mohan K. Balasubramanian, and Masanori Mishima. 2020. "Polar Relaxation by Dynein-Mediated Removal of Cortical Myosin II." *The Journal of Cell Biology* 219 (8). https://doi.org/10.1083/jcb.201903080.

Charras, Guillaume, and Ewa Paluch. 2008. "Blebs Lead the Way: How to Migrate without Lamellipodia." *Nature Reviews. Molecular Cell Biology* 9 (9): 730–36.

Du, Guangwei, and Michael A. Frohman. 2009. "A Lipid-Signaled Myosin Phosphatase Surge Disperses Cortical Contractile Force Early in Cell Spreading." *Molecular Biology of the Cell* 20 (1): 200–208.

Even-Ram, Sharona, Andrew D. Doyle, Mary Anne Conti, Kazue Matsumoto, Robert S. Adelstein, and Kenneth M. Yamada. 2007. "Myosin IIA Regulates Cell Motility and Actomyosin-Microtubule Crosstalk." *Nature Cell Biology* 9 (3): 299–309.

Girard, Kristine D., Charles Chaney, Michael Delannoy, Scot C. Kuo, and Douglas N. Robinson. 2004. "Dynacortin Contributes to Cortical Viscoelasticity and Helps Define the Shape Changes of Cytokinesis." *The EMBO Journal* 23 (7): 1536–46.

Green, Rebecca A., Ewa Paluch, and Karen Oegema. 2012. "Cytokinesis in Animal Cells." *Annual Review of Cell and Developmental Biology* 28 (1): 29–58.

Guglielmi, Giorgia, Joseph D. Barry, Wolfgang Huber, and Stefano De Renzis. 2015. "An Optogenetic Method to Modulate Cell Contractility during Tissue Morphogenesis." *Developmental Cell* 35 (5): 646–60.

Guntas, Gurkan, Ryan A. Hallett, Seth P. Zimmerman, Tishan Williams, Hayretin Yumerefendi, James E. Bear, and Brian Kuhlman. 2015. "Engineering an Improved Light-Induced Dimer (iLID) for Controlling the Localization and Activity of Signaling Proteins." *Proceedings of the National Academy of Sciences of the United States of America* 112 (1): 112–17.

Heissler, Sarah M., and Dietmar J. Manstein. 2013. "Nonmuscle Myosin-2: Mix and Match." *Cellular and Molecular Life Sciences: CMLS* 70 (1): 1–21.

Hirano, K., B. C. Phan, and D. J. Hartshorne. 1997. "Interactions of the Subunits of Smooth Muscle Myosin Phosphatase." *The Journal of Biological Chemistry* 272 (6): 3683–88.

561 Houk, Andrew R., Alexandra Jilkine, Cecile O. Mejean, Rostislav Boltyanskiy, Eric R. Dufresne,

562 Sigurd B. Angenent, Steven J. Altschuler, Lani F. Wu, and Orion D. Weiner. 2012. "Membrane

563 Tension Maintains Cell Polarity by Confining Signals to the Leading Edge during Neutrophil

564 Migration." *Cell* 148 (1-2): 175–88.

565 Ito, Masaaki, Takeshi Nakano, Ferenc Erd, and David J. Hartshorne. 2004. "Myosin Phosphatase:

566 Structure, Regulation and Function." *Molecular and Cellular Biochemistry* 259: 197–209.

567 Izquierdo, Emiliano, Theresa Quinkler, and Stefano De Renzis. 2018. "Guided Morphogenesis

568 through Optogenetic Activation of Rho Signalling during Early Drosophila Embryogenesis."

569 *Nature Communications* 9 (1): 2366.

570 Kelkar, Manasi, Pierre Bohec, and Guillaume Charras. 2020. "Mechanics of the Cellular Actin

571 Cortex: From Signalling to Shape Change." *Current Opinion in Cell Biology* 66 (June): 69–78.

572 Kennedy, Matthew J., Robert M. Hughes, Leslie A. Peteya, Joel W. Schwartz, Michael D. Ehlers,

573 and Chandra L. Tucker. 2010. "Rapid Blue-Light-Mediated Induction of Protein Interactions in

574 Living Cells." *Nature Methods* 7 (12): 973–75.

575 Khaliullin, Renat N., Rebecca A. Green, Linda Z. Shi, J. Sebastian Gomez-Cavazos, Michael W.

576 Berns, Arshad Desai, and Karen Oegema. 2018. "A Positive-Feedback-Based Mechanism for

577 Constriction Rate Acceleration during Cytokinesis in Caenorhabditis Elegans." *eLife* 7 (July).

578 https://doi.org/10.7554/eLife.36073.

579 Kimura, K., M. Ito, M. Amano, K. Chihara, Y. Fukata, M. Nakafuku, B. Yamamori, et al. 1996.

580 "Regulation of Myosin Phosphatase by Rho and Rho-Associated Kinase (Rho-Kinase)." *Science*

581 273 (5272): 245–48.

582 Krueger, Daniel, Emiliano Izquierdo, Ranjith Viswanathan, Jonas Hartmann, Cristina Pallares

583 Cartes, and Stefano De Renzis. 2019. "Principles and Applications of Optogenetics in

584 Developmental Biology." *Development* 146 (20). https://doi.org/10.1242/dev.175067.

585 Levskaya, Anselm, Orion D. Weiner, Wendell A. Lim, and Christopher A. Voigt. 2009.

586 "Spatiotemporal Control of Cell Signalling Using a Light-Switchable Protein Interaction." *Nature*

587 461 (7266): 997–1001.

588 Martin, Katrin, Andreas Reimann, Rafael D. Fritz, Hyunryul Ryu, Noo Li Jeon, and Olivier Pertz.

589 2016. "Spatio-Temporal Co-Ordination of RhoA, Rac1 and Cdc42 Activation during Prototypical

590 Edge Protrusion and Retraction Dynamics." *Scientific Reports* 6 (February): 21901.

591 Matthews, Helen K., Sushila Ganguli, Katarzyna Plak, Anna V. Taubenberger, Zaw Win, Max

592 Williamson, Matthieu Piel, Jochen Guck, and Buzz Baum. 2020. "Oncogenic Signaling Alters Cell

593 Shape and Mechanics to Facilitate Cell Division under Confinement." *Developmental Cell* 52 (5):

594 563–73.e3.

595 Mukhina, Svetlana, Yu-Li Wang, and Maki Murata-Hori. 2007. "Alpha-Actinin Is Required for

596   Tightly Regulated Remodeling of the Actin Cortical Network during Cytokinesis." *Developmental*

597   *Cell* 13 (4): 554–65.

598   Narumiya, Shuh, Masahiro Tanji, and Toshimasa Ishizaki. 2009. "Rho Signaling, ROCK and

599   mDia1, in Transformation, Metastasis and Invasion." *Cancer Metastasis Reviews* 28 (1-2): 65–76.

600   Natwick, Dean E., and Sean R. Collins. 2021. "Optimized iLID Membrane Anchors for Local

601   Optogenetic Protein Recruitment." *ACS Synthetic Biology*, April.

602   https://doi.org/10.1021/acssynbio.0c00511.

603   Niwa, H., K. Yamamura, and J. Miyazaki. 1991. "Efficient Selection for High-Expression

604   Transfectants with a Novel Eukaryotic Vector." *Gene* 108 (2): 193–99.

605   Oakes, Patrick W., Elizabeth Wagner, Christoph A. Brand, Dimitri Probst, Marco Linke, Ulrich S.

606   Schwarz, Michael Glotzer, and Margaret L. Gardel. 2017. "Optogenetic Control of RhoA Reveals

607   Zyxin-Mediated Elasticity of Stress Fibres." *Nature Communications* 8 (June): 15817.

608   O'Connell, C. B., A. K. Warner, and Y. Wang. 2001. "Distinct Roles of the Equatorial and Polar

609   Cortices in the Cleavage of Adherent Cells." *Current Biology: CB* 11 (9): 702–7.

610   Oshiro, Noriko, Yuko Fukata, and Kozo Kaibuchi. 1998. "Phosphorylation of Moesin by Rho-

611   Associated Kinase (Rho-Kinase) Plays a Crucial Role in the Formation of Microvilli-like Structures

612   *." *The Journal of Biological Chemistry* 273 (52): 34663–66.

613   Paluch, Ewa K., Irene M. Aspalter, and Michael Sixt. 2016. "Focal Adhesion-Independent Cell

614   Migration." *Annual Review of Cell and Developmental Biology* 32 (October): 469–90.

615   Reymann, Anne-Cecile, Fabio Staniscia, Anna Erzberger, Guillaume Salbreux, and Stephan W.

616   Grill. 2016. "Cortical Flow Aligns Actin Filaments to Form a Furrow." *eLife* 5 (October).

617   https://doi.org/10.7554/eLife.17807.

618   Ridley, Anne J., Martin A. Schwartz, Keith Burridge, Richard A. Firtel, Mark H. Ginsberg, Gary

619   Borisy, J. Thomas Parsons, and Alan Rick Horwitz. 2003. "Cell Migration: Integrating Signals from

620   Front to Back." *Science* 302 (5651): 1704–9.

621   Rodrigues, Nelio T. L., Sergey Lekomtsev, Silvana Jananji, Janos Kriston-Vizi, Gilles R. X.

622   Hickson, and Buzz Baum. 2015. "Kinetochore-Localized PP1-Sds22 Couples Chromosome

623   Segregation to Polar Relaxation." *Nature* 524 (7566): 489–92.

624   Saitoh, M., T. Ishikawa, S. Matsushima, M. Naka, and H. Hidaka. 1987. "Selective Inhibition of

625   Catalytic Activity of Smooth Muscle Myosin Light Chain Kinase." *The Journal of Biological*

626   *Chemistry* 262 (16): 7796–7801.

627   Sedzinski, Jakub, Maté Biro, Annelie Oswald, Jean Yves Tinevez, Guillaume Salbreux, and Ewa

628   Paluch. 2011. "Polar Actomyosin Contractility Destabilizes the Position of the Cytokinetic

629   Furrow." *Nature* 476 (7361): 462–68.

630   Straight, Aaron F., Amy Cheung, John Limouze, Irene Chen, Nick J. Westwood, James R. Sellers,

631   and Timothy J. Mitchison. 2003. "Dissecting Temporal and Spatial Control of Cytokinesis with a

632   Myosin II Inhibitor." *Science* 299 (5613): 1743–47.

633   Taneja, Nilay, Matthew R. Bersi, Sophie M. Baillargeon, Aidan M. Fenix, James A. Cooper,

634   Ryoma Ohi, Vivian Gama, W. David Merryman, and Dylan T. Burnette. 2020. "Precise Tuning of

635   Cortical Contractility Regulates Cell Shape during Cytokinesis." *Cell Reports* 31 (1): 107477.

636   Tinevez, Jean-Yves, Ulrike Schulze, Guillaume Salbreux, Julia Roensch, Jean-François Joanny, and

637   Ewa Paluch. 2009. "Role of Cortical Tension in Bleb Growth." *Proceedings of the National*

638   *Academy of Sciences of the United States of America* 106 (44): 18581–86.

639   Totsukawa, Go, Yue Wu, Yasuharu Sasaki, David J. Hartshorne, Yoshihiko Yamakita, Shigeko

640   Yamashiro, and Fumio Matsumura. 2004. "Distinct Roles of MLCK and ROCK in the Regulation

641   of Membrane Protrusions and Focal Adhesion Dynamics during Cell Migration of Fibroblasts." *The*

642   *Journal of Cell Biology* 164 (3): 427–39.

643   Tse, Justin R., and Adam J. Engler. 2010. "Preparation of Hydrogel Substrates with Tunable

644   Mechanical Properties." *Current Protocols in Cell Biology / Editorial Board, Juan S. Bonifacino ...*

645   *[et Al.]* Chapter 10 (June): Unit 10.16.

646   Turlier, Hervé, Basile Audoly, Jacques Prost, and Jean-François Joanny. 2014. "Furrow

647   Constriction in Animal Cell Cytokinesis." *Biophysical Journal* 106 (1): 114–23.

648   Uda, Youichi, Yuhei Goto, Shigekazu Oda, Takayuki Kohchi, Michiyuki Matsuda, and Kazuhiro

649   Aoki. 2017. "Efficient Synthesis of Phycocyanobilin in Mammalian Cells for Optogenetic Control

650   of Cell Signaling." *Proceedings of the National Academy of Sciences* 114 (45): 11962–67.

651   Uehata, M., T. Ishizaki, H. Satoh, T. Ono, T. Kawahara, T. Morishita, H. Tamakawa, et al. 1997.

652   "Calcium Sensitization of Smooth Muscle Mediated by a Rho-Associated Protein Kinase in

653   Hypertension." *Nature* 389 (6654): 990–94.

654   Valon, Léo, Ariadna Marín-Llauradó, Thomas Wyatt, Guillaume Charras, and Xavier Trepat. 2017.

655   "Optogenetic Control of Cellular Forces and Mechanotransduction." *Nature Communications* 8

656   (February): 14396.

657   Vicente-Manzanares, M., X. Ma, R. S. Adelstein, and A. R. Horwitz. 2009. "Non-Muscle Myosin II

658   Takes Centre Stage in Cell Adhesion and Migration." *Nature reviews.Molecular Cell Biology* 10

659   (11): 778–90.

660   Wagner, Elizabeth, and Michael Glotzer. 2016. "Local RhoA Activation Induces Cytokinetic

661   Furrows Independent of Spindle Position and Cell Cycle Stage." *The Journal of Cell Biology* 213

662   (6): 641–49.

663   Worthylake, Rebecca A., and Keith Burridge. 2003. "RhoA and ROCK Promote Migration by

664   Limiting Membrane Protrusions *." *The Journal of Biological Chemistry* 278 (15): 13578–84.

665   Wu, Yue, Andrea Murányi, Ferenc Erdodi, and David J. Hartshorne. 2005. "Localization of Myosin

23

666   Phosphatase Target Subunit and Its Mutants." *Journal of Muscle Research and Cell Motility* 26 (2-
667   3): 123–34.

668   Yamamoto, Kei, Kohei Otomo, Tomomi Nemoto, Seiichiro Ishihara, Hisashi Haga, Akira
669   Nagasaki, Yota Murakami, and Masayuki Takahashi. 2019. "Differential Contributions of
670   Nonmuscle Myosin IIA and IIB to Cytokinesis in Human Immortalized Fibroblasts." *Experimental*
671   *Cell Research*. https://doi.org/10.1016/j.yexcr.2019.01.020.

672   Yoneda, M., and K. Dan. 1972. "Tension at the Surface of the Dividing Sea-Urchin Egg." *The*
673   *Journal of Experimental Biology* 57 (3): 575–87.

674   Yonemura, Shigenobu, Takeshi Matsui, Shoichiro Tsukita, and Sachiko Tsukita. 2002. "Rho-
675   Dependent and -Independent Activation Mechanisms of Ezrin/radixin/moesin Proteins: An
676   Essential Role for Polyphosphoinositides in Vivo." *Journal of Cell Science* 115 (Pt 12): 2569–80.

677   Yusa, Kosuke, Liqin Zhou, Meng Amy Li, Allan Bradley, and Nancy L. Craig. 2011. "A
678   Hyperactive piggyBac Transposase for Mammalian Applications." *Proceedings of the National*
679   *Academy of Sciences of the United States of America* 108 (4): 1531–36.